

# Supplementary Material

## 1 Drivers description

Table S1. List of drivers currently available on *eDrivers* along with their respective acronym used in the figures in the supplementary material.

Groups	Drivers	Acronym	Source
Climate	Aragonite	ACID	(Starr and Chassé, 2019)
Climate	Hypoxia	HYP	(Blais et al., 2019)
Climate	Sea bottom temperature	SBT-	(Galbraith et al., 2018)
Climate	Sea bottom temperature	SBT+	(Galbraith et al., 2018)
Climate	Sea level rise	SLR	(Halpern et al., 2015a)
Climate	Sea surface temperature	SST-	(Galbraith et al., 2018)
Climate	Sea surface temperature	SST+	(Galbraith et al., 2018)
Coastal	Aquaculture	AQUA	(AAF, 2016; DFO, 2016a; FA, 2016; FFA, 2016; MAPAQ, 2016)
Coastal	Coastal development	CD	(Earth observation group, 2019)
Coastal	Direct human impact	DHI	(Statistics-Canada, 2017)
Coastal	Inorganic pollution	IP	(Halpern et al., 2015a)
Coastal	Nutrient import	NI	(Halpern et al., 2015a)
Coastal	Organic pollution	OP	(Halpern et al., 2015a)
Coastal	Toxic algae	TA	(Bates et al., 2019)
Fisheries	Demersal, destructive	DD	(DFO, 2016b)
Fisheries	Demersal, non-destructive, high-bycatch	DNH	(DFO, 2016b)

Groups	Drivers	Acronym	Source
Fisheries	Demersal, non-destructive, low-bycatch	DNL	(DFO, 2016b)
Fisheries	Pelagic, high-bycatch	PHB	(DFO, 2016b)
Fisheries	Pelagic, low-bycatch	PLB	(DFO, 2016b)
Marine traffic	Invasive species	INV	(Halpern et al., 2015a)
Marine traffic	Marine pollution	MP	(Halpern et al., 2015a)
Marine traffic	Shipping	SHP	(Halpern et al., 2015a)

## 1.1 Climate

### 1.1.1 Acidification

Oceans are the largest reservoir and sink of atmospheric carbon dioxide ( $CO_2$ ). Its uptake increases seawater acidity and the lowers saturation state with respect to calcite ( $\Omega_C$ ) and aragonite ( $\Omega_A$ ), the two most common  $CaCO_3$  polymorphs constituting the shells and skeleton of many marine organisms (Mucci et al., 2017). This can have deleterious effects on carbonate-secreting organisms (*e.g.* mollusks and crustaceans) and certain physiological processes in non-calcifying organisms (Fabry et al., 2008; Kroeker et al., 2013).

When  $\Omega_C$  or  $\Omega_A$  decrease below 1, water becomes undersaturated and corrosive to the skeletal minerals of carbonate-secreting organisms. Note that if  $\Omega_A < 1$ , the waters may still be supersaturated with respect to calcite since it is 50% more soluble than aragonite. However, organisms have wide ranging responses to  $\Omega_C$  and  $\Omega_A$  saturation state. For example, most corals stop calcifying at  $\Omega_A < 2$  (Bove et al., 2019; Kleypas et al., 2006), while other organisms may have adapted to precipitate  $CaCO_3$  even when seawater is undersaturated with respect to calcite ( $\Omega_C < 1$  or  $\Omega_A < 0.65$ ; *e.g.* Uthicke et al., 2016).

We used  $\Omega_A$  saturation state to characterize ocean acidification in the bottom waters of the St. Lawrence. The data come from the Department of Fisheries and Oceans' (DFO) Atlantic Zone Monitoring Program (AZMP; Galbraith et al., 2018) surveys and DFO's multispecies surveys (Bourdages et al., 2018) collected in August-September of 2017 (Starr and Chassé,

2019). The carbonate chemistry was determined through pH and TA measurements. Samples for pH and total alkalinity (TA) were collected under a bubble free and no head space conditions into 500 mL borosilicate glass flasks, 250  $\mu$ L of the saturated  $HgCl_2$  solution was added to sample, and processed following the “Guide to best practices for Ocean CO<sub>2</sub> Measurements” (Dickson et al., 2007).

$pH_T$  was determined spectrophotometrically using the indicator dye m-cresol purple (Sigma-Aldrich). Absorbance was measured at 730, 578 and 434 nm before and after dye addition in 10 cm quartz cells thermostated at  $25 \pm 0.05^\circ C$  (Dickson et al., 2007). A similar procedure was carried out before each set of sample measurements using a TRIS (Tris (hydroxymethyl)-aminomethane) buffer prepared at a practical salinity (S) of approximately 30 (Millero, 1986). Certified Reference Material (CRM) (supplied by Professor Andrew Dickson, Scripps Institution of Oceanography, San Diego, USA) was used for quality control of our pH TRIS buffer.

TA was determined by potentiometric titration in an open cell using an automated Radiometer potentiometric titrator (Titrilab 865) and a pH combination electrode (pHC2001) in a continuous titrant addition mode, an algorithm specifically designed for shallow end-point detection (Dickson et al., 2007). The dilute HCl titrant 0.1M in a solution of NaCl of 0.6M was calibrated using CRM provided by Professor Andrew G. Dickson.

The carbonate system parameters (including  $\Omega_A$ ) were corrected for in situ pressure and temperature using the algorithm CO<sub>2</sub>SYS (Lewis et al., 1998) with measured pH, total alkalinity, soluble reactive and silicate concentrations as input parameters.

$\Omega_A$ , pH, dissolved oxygen ( $O_2$ ) and pressure were sampled at 117 stations in the Estuary and Gulf of St. Lawrence in the summer of 2018. The majority of sampling stations were located in the Southern Gulf ( $n = 84$ ), compared to the Estuary and Northern Gulf ( $n = 33$ ).

To account for low sample size in the Northern Gulf, we used the correlation between  $O_2$  and  $CO_2$ , which are linked through the stoichiometry of the respiration reaction in waters that are isolated from the atmosphere (Mucci et al., 2011). Metabolic  $CO_2$  increases in water through biotic processes such microbial respiration of organic matter (Mucci et al., 2011). In deep waters, variations of  $\Omega_A$  are largely governed by the addition of metabolic  $CO_2$ , whereas near the air-sea interface  $O_2$  is replenished faster than  $CO_2$  can escape (Zeebe and Wolf-Gladrow, 2001). The impact of respiration on carbonate chemistry is highest in hypoxic regions, where metabolic  $CO_2$  accumulates to high concentrations (Mucci et al., 2011).

We explored the correlation between  $\Omega_A$  and  $O_2$  in the data and found no significant cor-

relation at the scale of the whole St. Lawrence ( $p$ -value: 0.08;  $R^2$ : 0.03). Nevertheless, a correlation between  $\Omega_A$  and  $O_2$  exists in the Northern St. Lawrence ( $p$ -value:  $< 0.01$ ;  $R^2$ : 0.49), but not in the Southern St. Lawrence ( $p$ -value: 0.85;  $R^2$ :  $< 0.01$ ). Furthermore, the correlation observed in the north between  $\Omega_A$  and  $O_2$  is especially strong when deep Channels (*Deep* model:  $p$ -value:  $< 0.01$ ;  $O_2$ : 0.20;  $R^2$ : 0.97) are separated from shallower regions (*Shallow* model:  $p$ -value:  $< 0.01$ ;  $O_2$ : 0.07;  $R^2$ : 0.96), with  $\Omega_A$  increasing more steeply with increasing  $O_2$  in deep Channels. This stronger correlation is likely caused by the lack of gas exchange with the atmosphere or the surface mixed layer and the importance of metabolic  $CO_2$  in deep waters, some of which may have mean ages of up to 20 years (Mucci et al., 2011). In the Northern Gulf, the acidification is following depth and distance from the Cabot Strait along the Laurentian, Anticosti and Esquiman Channels due to the progressive oxygen depletion and metabolic carbon dioxide accumulation (Mucci et al., 2011).

There are likely different dynamics at play in the Southern Gulf, such as waters with lowered alkalinity and salinity caused by the St. Lawrence plume. Such water masses are have lower buffering capacities to decreasing pH and  $\Omega_A$ . Also, the accumulation of metabolic carbon dioxide produced by rapid oxic degradation of organic matter in the sandy and permeable sediments of the Magdalen Shelf or through the St. Lawrence plume could decrease  $\Omega_A$  in the Southern Gulf (Starr and Chassé, *personal communication*).

We thus divided the analyses between the Southern and Northern St. Lawrence. The St. Lawrence was divided using the 350m isobath on the southern slope of the Laurentian Channel, from the Cabot Strait to the tip of the Gaspé Peninsula.  $\Omega_A$  distribution in the Southern St. Lawrence was modelled using the exponential kriging model.

We predicted  $\Omega_A$  using  $O_2$  for the Northern St. Lawrence. Whereas there are few published datasets on  $\Omega_A$  in the St. Lawrence, there is a robust time-series on oxygen concentration in the water column from the Department of Fisheries and Oceans' (DFO) Atlantic Zone Monitoring Program (AZMP; Galbraith et al., 2018). We used oxygen concentration data collected between 2013 and 2017 (Blais et al., 2019) and interpolated oxygen % saturation using cokriging with depth as a covariable, as done in (Dutil et al., 2011). Bathymetric data come from Dutil et al. (2011) and have a 100  $km^2$  resolution. For more details, refer to the hypoxia description. The *Deep* model was used to transform  $O_2$  values to  $\Omega_A$  in grid cells with depth  $> 350m$ , while the *Shallow* model was applied to cells with depth  $< 350m$ .

Based on the wide range of  $\Omega_A$  levels at which organism are negatively affected (see above), we built an index of acidification stress ( $A_s$ ) ranging between 0 and 1 that slowly begins increasing as  $\Omega_A \approx 2$ , increases more rapidly close to  $\Omega_A = 1$  and reaches its peak at  $\Omega_A \approx 0.5$ :

$$A_s = \frac{-3}{.99 + e^{-2*\Omega_A}} + 3$$

Hence, the higher the acidification stress, the higher the index of acidification becomes.

### 1.1.2 Hypoxia

The data used to characterize hypoxia uses oxygen saturation in % and come from the Department of Fisheries and Oceans' (DFO) Atlantic Zone Monitoring Program (AZMP; Galbraith et al., 2018) surveys in late spring and fall, as well as from annual DFO's multi-species surveys for the northern Gulf in August and for the Magdalen Shallows in September. We provide a brief summary of data and methods to describe hypoxia in this document. For more details, refer to Blais et al. (2019).

Oxygen concentration is measured at every station using an oxygen probe (Sea-Bird SBE43) mounted on the CTD. The probe is calibrated against seawater samples that are analyzed by Winkler titration on every cast (see Blais et al., 2019 for calibration procedure). The data used is the last depth sampled on the CTD profile, which typically corresponds to ~10m above the bottom. Oxygen concentration ( $\mu M L^{-1}$ ) is converted to oxygen saturation taking into account the salinity and temperature at the selected depth.

We interpolated oxygen saturation using cokriging with depth as a covariable, as done in (Dutil et al., 2011). Bathymetric data come from Dutil et al. (2011) and have a 100  $km^2$  resolution. According to Diaz and Rosenberg (1995), severe hypoxia can be observed when dissolved oxygen falls below 2  $ml L^{-1}$ , which corresponds to 62.5  $\mu mol L^{-1}$  and ~20% saturation. This is considered as the level necessary to maintain most animal life. Similarly, Chabot and Claireaux (2008) studied the effects of hypoxia on the energy budget of cod in the St. Lawrence and found that behavioural effects began manifesting below 70% oxygen saturation and that survival becomes jeopardized below ~20% saturation. We used these observations to create an index of hypoxia using an inverted logistic curve that slowly increases below 70% oxygen saturation, increases acutely as it approaches the 20% oxygen saturation threshold and reaches its peak intensity between 20 and 30% oxygen saturation:

$$H_s = \frac{-1}{.99 + 200 * e^{-0.15*O_2}} + 1$$

Hence, the higher the hypoxic stress, the higher the index of hypoxia becomes.

### 1.1.3 Bottom temperature anomalies

The data used to characterize bottom temperature anomalies come from the Department of Fisheries and Oceans' (DFO) Atlantic Zone Monitoring Program (AZMP; Galbraith et al., 2018). We provide a brief summary of data and methods to characterize the bottom temperature climatology and anomalies in this document. For more details, refer to Galbraith et al. (2018).

Bottom temperatures are interpolated in the Gulf using conductivity-temperature-depth (CTD) sampling performed annually through DFO's multispecies surveys for the northern Gulf in August and for the Magdalen Shallows in September. Using this sampling survey, temperatures are horizontally interpolated at each 1 m depth layer on a 2 km resolution grid. Bottom temperatures are then extracted by using a bathymetry layer from the Canadian Hydrographic Survey (Dutil et al., 2012) and selecting the interpolated temperature from the layer corresponding to the bottom depth at each grid point.

We used temperature anomalies, *i.e.* deviations from long-term normal conditions, to measure an annual index of stress associated with extreme temperatures between 2013 and 2017. Temperature anomalies were calculated using the difference between grid cell values with 1981-2010 climatological averages. Anomaly time series were normalized by their standard deviation (SD) to allow comparison between areas of the St. Lawrence with different temperature ranges. For example, temperatures observed in deep channels are less variable than in shallower regions of the St. Lawrence. Hence, if anomalies were expressed in degrees Celsius, it would underestimate the relative importance of anomalies in deep channels when compared to shallower regions. Grid cells whose monthly value exceeded  $\pm 0.5$  standard deviation (SD) from the long-term average were considered as anomalous (Galbraith et al., 2018). Outliers in the data were defined as those that fell beyond the interquartile range \* 3, identified as extreme outliers by Tukey (1977). Outlier values were capped to correspond to the 5th and 95th percentiles. Anomalies were divided into positive and negative anomalies and the absolute value of anomalies were used as an indicator of the intensity of bottom temperature anomalies. The mean anomaly intensity between 2013 and 2017 for each grid cell was used to generate the final index of bottom temperature anomalies.

### 1.1.4 Surface temperature anomalies

The data used to characterize surface temperature anomalies come from the Department of Fisheries and Oceans' (DFO) Atlantic Zone Monitoring Program (AZMP; Galbraith et al., 2018). We provide a brief summary of data and methods to characterize the surface tem-

perature climatology and anomalies in this document. For more details, refer to Galbraith et al. (2018).

The surface layer is characterized using sea surface temperature (SST) monthly composites from Advanced Very High Resolution Radiometer (AVHRR) satellite images obtained from the National Oceanic and Atmospheric Administration (NOAA) and European Organization for the Exploitation of Meteorological Satellites (EUMETSAT). Images used are from DFO's Maurice Lamontagne Institute at a 1 km resolution from 1985-2013 and from DFO's Bedford Institute of Oceanography (BIO) Operational Remote Sensing group at a 1.5 km resolution since 2014. Monthly anomalies were constructed as the difference between monthly averages and the 1985-2010 climatological mean for each month.

Surface temperature anomalies were characterized following the same method used for bottom temperature anomalies. Only the months of May to November were included to avoid biases associated with the presence of ice cover. Monthly anomalies from May to November values were summed to obtain an indicator of annual surface temperature anomaly intensity in each grid cell. The mean anomaly intensity between 2013 and 2017 for each grid cell was used to generate the final index of surface temperature anomalies.

#### **1.1.5 Sea level rise**

The data used to characterize sea level rise risk comes from the global cumulative impacts assessment on habitats (Halpern et al., 2015b, 2008) and available on the NCEAS online data repository (Halpern et al., 2015a). We provide a brief summary of data and methods in this document. For more details, refer to Halpern et al. (2015a).

Sea level rise was characterized by Nicholls and Cazenave (2010) using NASA's satellite altimetry data (Topex/Poseidon, Jason-1&2, GFO, ERS-1&2, and Envisat missions) and available at <http://www.aviso.altimetry.fr/en/data/products/ocean-indicatorsproducts/mean-sea-level/products-images.html>

The rate of sea level rise ( $mm/year$ ) was measured between 1992 and 2012 and transformed as a net change value ( $mm$ ) by multiplying by the number of years considered. Only positive values were selected under the assumption that only positive sea level rise is likely to cause environmental stress.

For the St. Lawrence, we overlaid the raw data layers (Halpern et al., 2015a) with our 1  $km^2$  grid cell using weighted area average.

## 1.2 Coastal

### 1.2.1 Aquaculture

Aquaculture data comes from a variety of sources in the St. Lawrence because aquaculture sites are mostly managed at the provincial level. We therefore had to gather the data on aquaculture sites from the 5 provinces dividing the St. Lawrence (AAF, 2016; DFO, 2016a; FA, 2016; FFA, 2016; MAPAQ, 2016).

Invertebrates aquaculture is especially important in the southern and western Gulf. Fish and algae aquaculture, on the other hand, remains marginal. Considering this, we only considered invertebrates aquaculture for the aquaculture driver layer. However, if fish or algae farming were to become more important, these driver should be incorporated in future analyses as individual layers, as impacts vary between types of aquaculture.

Aquaculture activities are highly localized and potential effects do not or rarely extend beyond the location of the farms. We therefore only considered the actual location of sites to characterize the distribution of this driver. We were unable to characterize site production in terms of biomass farmed, which could provide an indication of the intensity of aquaculture activities. As such, we considered aquaculture as binary presence-absence data in our analyses.

### 1.2.2 Coastal development

We used lights at night as a proxy of coastal infrastructure development, as terrestrial stable lights at night represent light from human settlements and industrial sites with electricity.

The data comes from the Nighttime Lights Time Series. Nighttime light products are compiled by the Earth Observation Group at the National Oceanic and Atmospheric Administration's (NOAA) National Centers for Environmental Information (NCEI). They use globally available nighttime data obtained from the Visible Infrared Imaging Radiometer Suite (VIIRS) Day/Night Band (DNB) of the Defense Meteorological Satellite Program (DMSP) to characterize global average radiance ( $\text{nanoWatts cm}^{-2} \text{ sr}^{-1}$ ) composite images at a 15 arc-second ( $\sim 200$  m) resolution.

We used the annual Version 1 Nighttime VIIRS DNB composites between 2015 and 2016 (Earth observation group, 2019) to characterize coastal development in coastal areas of the St. Lawrence. As the effects of coastal development are likely acute in its direct vicinity, we extracted average radiance values using a 2 km buffer around grid cells within 2 km of the coast. We used a weighted area average to extract the radiance values.



### 1.2.3 Direct human impact

As in Halpern et al. (2008) and Halpern et al. (2015a), we used the sum of coastal populations as a proxy of direct human impact. We used Statistics Canada dissemination area population count from the 2016 census to obtain coastal population size around the St. Lawrence (Statistics-Canada, 2017). Dissemination areas are the smallest standard geographic area in which census data are disseminated and they combine to cover all of Canada. The census provides population count within the boundary of each dissemination area, which we used to evaluate total coastal population.

As the effects of direct human impacts are likely acute mostly in coastal areas we calculated total population in grid cells within 2 km of the coast. Total population was measured in a 10 km buffer around each coastal cell. The total population in each buffer was the sum of intersecting dissemination areas divided by the intersection area between buffers and dissemination areas:

$$DHI_j = \sum_{k=1}^{n_j} P_k * \frac{A_{j,k}}{A_{tot,k}}$$

where  $j$  is a buffered grid cell,  $k$  is a dissemination area intersecting  $j$ ,  $P$  is the population in  $k$ ,  $A$  is the area of the  $k$  overlapping with  $j$  and  $A_{tot}$  is the total area of  $k$ . This approach was favoured to reduce the effects of very large dissemination areas overlapping with buffers on a very small percentage of their total area.

### 1.2.4 Inorganic pollution

The data used to characterize inorganic pollution comes from the global cumulative impacts assessment on habitats (Halpern et al., 2015b, 2008) and available on the NCEAS online data repository (Halpern et al., 2015a). We provide a brief summary of data and methods in this document. For more details, refer to Halpern et al. (2015a).

Inorganic pollution was modelled using impervious surface area (*i.e.* artificial surfaces such as paved roads) under the assumption that most of this pollution source comes from urban runoff. Inorganic pollution originating from point-sources or in areas lacking paved roads is therefore not captured by this layer. The data obtained was aggregated at the watershed scale and spread into coastal and marine environments was modelled using a diffusive plume model from each watershed pourpoints (*e.g.* river mouths).

For the St. Lawrence, we overlaid the raw data layers (Halpern et al., 2015a) with our 1  $km^2$  grid cell using weighted area average.

### 1.2.5 Nutrient pollution

The data used to characterize nutrient pollution comes from the global cumulative impacts assessment on habitats (Halpern et al., 2015b, 2008) and available on the NCEAS online data repository (Halpern et al., 2015a). We provide a brief summary of data and methods in this document. For more details, refer to Halpern et al. (2015a).

Annual fertilizer use in tonnes ( $t$ ) was used as a proxy of nutrient pollution. The data used came from the Food and Agriculture Organization of the United Nations (FAO). Gaps in data were modelled using a linear regression between fertilizer and pesticides or agricultural gross domestic product (GDP). Dasymetric maps were then used to distribute fertilizer data over the landscape using 2009 data from the Moderate Resolution Imaging Spectroradiometer (MODIS) at  $\sim 500$  m resolution and aggregated to watersheds. Diffusive plume models from each watershed pourpoint (*e.g.* river mouths) were then used to model the distribution and intensity of nutrient pollution in coastal and marine environments.

For the St. Lawrence, we overlaid the raw data layers (Halpern et al., 2015a) with our 1  $km^2$  grid cell using weighted area average.

### 1.2.6 Organic pollution

The data used to characterize organic pollution comes from the global cumulative impacts assessment on habitats (Halpern et al., 2015b, 2008) and available on the NCEAS online data repository (Halpern et al., 2015a). We provide a brief summary of data and methods in this document. For more details, refer to Halpern et al. (2015a).

Annual pesticide use in tonnes ( $t$ ) was used as a proxy of organic pollution. The data used came from the FAO and gaps in data were modelled using a linear regression between pesticides and fertilizers or agricultural GDP. The same methodology as that used to characterized nutrient pollution was then applied to organic pollution.

For the St. Lawrence, we overlaid the raw data layers (Halpern et al., 2015a) with our 1  $km^2$  grid cell using weighted area average.

### 1.2.7 Toxic algae

The data we use to describe the risk of toxic algae comes from an expert based map delineating the areas where coastal areas are at risk from five different toxins (Bates et al., 2019). The map presents coastal areas at risk from 5 different toxins: 1) paralytic shellfish poisoning (PSP) toxins from the regular presence of the dinoflagellate *Alexandrium catenella* (previously *Alexandrium tamarense*) at high concentrations, 2) amnesic shellfish poisoning (ASP) toxins from domoic acid 3) diarrhetic shellfish poisoning (DSP) toxins, 4) spirolides and 5) pectenotoxins, two toxins produced by dinoflagellates occurring in the St. Lawrence.

The information provided on this expert map on the 5 toxins (Bates et al., 2019). was georeferenced and transformed as vectorized objects. We calculated a toxic algae risk ( $T$ ) index for each cell ( $x$ ) in the  $1\text{ km}^2$  study grid. For each toxin ( $t$ ), a value of 1 was attributed to all grid cells overlapping with areas identified at risk on the expert map and a value of 0.5 for grid cells overlapping with areas where ASP and DSP toxins were observed without exceeding legal thresholds. The value for all 5 toxins was then summed for all grid cells:

$$TA_{i,x} = \sum_{i=1}^5 i_x$$

## 1.3 Fisheries

The impacts of fisheries activities in the St. Lawrence are evaluated using DFO’s fisheries logbooks program (DFO, 2016b). While logbooks are not mandatory for all fisheries in the St. Lawrence, they still provide a very thorough overview of the spatial distribution and intensity of fishing activities in the St. Lawrence. The data we used spans 6 years from 2010 to 2015 and details 218323 fishing events ( $36387 \pm 3147$  fishing events per year). There were 31 targeted species and a total of 53 caught species in the dataset.

Fishing activities are performed using a variety of gear types: trap, trawl, dredge, driftnet, hand line, longline, scuba diving, purse seine, seine, beach seine and jig fishing. Intensity of fishing activities was divided among gear types and based on their respective types of environmental impacts (Table S2). For example, traps and trawls have very different effects on a system. Gear classification was done using the classification presented in Halpern et al. (2008) and Halpern et al. (2015a) and is broken down into 5 distinct classes: demersal destructive (DD), demersal, non-destructive, low-bycatch (DNL), demersal, non-destructive, high-bycatch (DNH), pelagic, low-bycatch (PLB) and pelagic, high-bycatch (PHB). This categorization therefore divides the fisheries data into 5 distinct driver layers characterizing

fishing activities.

Gear types can also be further classified into fixed or mobile engines based on their mobility. We used these two mobility classes to generate a buffer of impact around each fishing activity coordinates to consider potential spatial uncertainty associated with locations and the fact that mobile engines can be tracted over several kilometers during fishing activities and that we do not have the beginning and end points of mobile fishing events. Buffer sizes for fixed and mobile engine was of 200 and 2000 meters, respectively.

Table S2. Classification of gear types in the fisheries dataset based on their environmental impact and mobility

Gear type (EN)	Classification	Mobility
Trap	DNH	Fixed
Trawl	DD	Mobile
Dredge	DD	Mobile
Driftnet	PHB	Fixed
Hand lines	PLB	Fixed
Longline	PHB	Fixed
Scuba diving	DNL	Fixed
Purse seine	PLB	Fixed
Seine	DNH	Fixed
Beach seine	DNH	Fixed
Trap	DNH	Fixed
Jig fishing	PLB	Fixed

In order to characterize the intensity of fishing activities ( $FI$ ), we used a biomass yield density index. We multiplied the total annual biomass captured in each grid cell  $j$ , regardless of species, by the proportion of fishing area in each grid cell:

$$FI_j = \sum_{k=1}^{n_j} B_{tot,k} * \frac{A_{j,k}}{A_{tot,k}}$$

where  $j$  is a grid cell,  $k$  is a fishing event,  $B_{tot}$  is the total biomass of a fishing event  $k$ ,  $A$  is the area of a fishing event  $k$  overlapping a cell  $j$  and  $A_{tot}$  is the total area of the fishing event  $k$ . This formula gives an intensity measurement in biomass units, which is kg in our case. Since we measure the intensity within a  $1 \text{ km}^2$  grid cell, the intensity evaluation is in  $\text{kg} * \text{km}^{-2}$ . This metric distributes the biomass captured within each grid cell as a function

of overlapping fishing area and provides an overview of how impacted each grid cell is in terms of extracted biomass.

## 1.4 Marine traffic

### 1.4.1 Shipping

The data used to characterize shipping comes from the global cumulative impacts assessment on habitats (Halpern et al., 2015b, 2008) and available on the NCEAS online data repository (Halpern et al., 2015a). We provide a brief summary of data and methods in this document. For more details, refer to Halpern et al. (2015a).

Two data sources were used to characterize shipping. The first set of data is gathered as part of the World Meteorological Organization Voluntary Observing Ships' (VOS) scheme. Ships participating in the program gather meteorological data along with observation location as part of an open-ocean climate dataset. The data spans 20 years and annually covers 10-20% of ships worldwide. Data used spanned 2003 to 2011.

The second set of data comes from the Automatic Identification System (AIS), an initiative launched in 2002 that sought to improve marine safety by providing mariners with real-time vessel traffic. Through the International Maritime Organization SOLAS agreement, all vessels of over 300 gross tonnage on international voyages and those carrying passengers are now required to be equipped with AIS transceivers. These transceivers use Global Positioning System technology to locate vessels every 10 minutes. The data used was from November 2010 to December 2011.

Data used come mostly from vessels that move globally (*i.e.* cargo, tanker and passenger), as they are required to carry AIS transceivers, but also include data from fishing, high-speed, pleasure and support classes. Shipping intensity was evaluated as the number of fishing tracks at a 0.1 decimal degrees resolution. For more details on data and methods used, consult (Walbridge, 2013).

For the St. Lawrence, we overlaid the raw data layers (Halpern et al., 2015a) with our 1  $km^2$  grid cell using weighted area average.

### 1.4.2 Invasive species

The data used to characterize invasive species risk comes from the global cumulative impacts assessment on habitats (Halpern et al., 2015b, 2008) and available on the NCEAS online data

repository (Halpern et al., 2015a). We provide a brief summary of data and methods in this document. For more details, refer to supplementary materials provided in Halpern et al. (2008) and Halpern et al. (2015a).

Cargo volume was used as a proxy of invasion risk under the assumption that risk of invasion is proportional to tonnes of goods transferred through ports. Cargo throughput in metric tonnes for the year 2011 was accessed through a variety of sources (see supplementary material in Halpern et al., 2015a for more details) and cross-matched with entries in the World Port Index database (WPI; available from the National Geospatial-Intelligence Agency). A gap-filling procedure using linear regression and sets of predictors related to port volume and available in the WPI dataset was then applied to the WPI dataset to predict missing cargo volume entries. Finally, volume data was distributed in marine environments adjacent to ports using a diffusive plume model with an exponential decay function that set the maximum spread distance to approximately 1000 km. The plume model was then clipped to areas less than 60 m deep, as invasive species are more likely to invade shallow areas.

For the St. Lawrence, we overlaid the raw data layers (Halpern et al., 2015a) with our 1  $km^2$  grid cell using weighted area average.

### 1.4.3 Marine pollution

The data used to characterize marine pollution risk comes from the global cumulative impacts assessment on habitats (Halpern et al., 2015b, 2008) and available on the NCEAS online data repository (Halpern et al., 2015a). Marine pollution was considered to be mainly driver by the shipping industry. As such, the driver layer was constructed by combining the shipping (*i.e.* shipping lanes) and invasive species (*i.e.* cargo volume) layers. For more details, refer to supplementary materials provided in Halpern et al. (2008) and Halpern et al. (2015a).

For the St. Lawrence, we overlaid the raw data layers (Halpern et al., 2015a) with our 1  $km^2$  grid cell using weighted area average.

## 2 Driver intensity and distribution

We evaluated the frequency distribution of each drivers to verify whether data should be transformed (Figure S1). In light of this, we log-transformed the following driver layers

- Coastal development

- Direct human impact
- All fisheries data
- Hypoxia
- Inorganic pollution
- Invasive species
- Nutrient pollution
- Organic pollution
- Sea bottom temperature anomalies
- Shipping

To allow for relative intensity comparison, all driver layers were subsequently normalized between 0 and 1 using the 99th quantile to further control for extreme values (Figure S2).

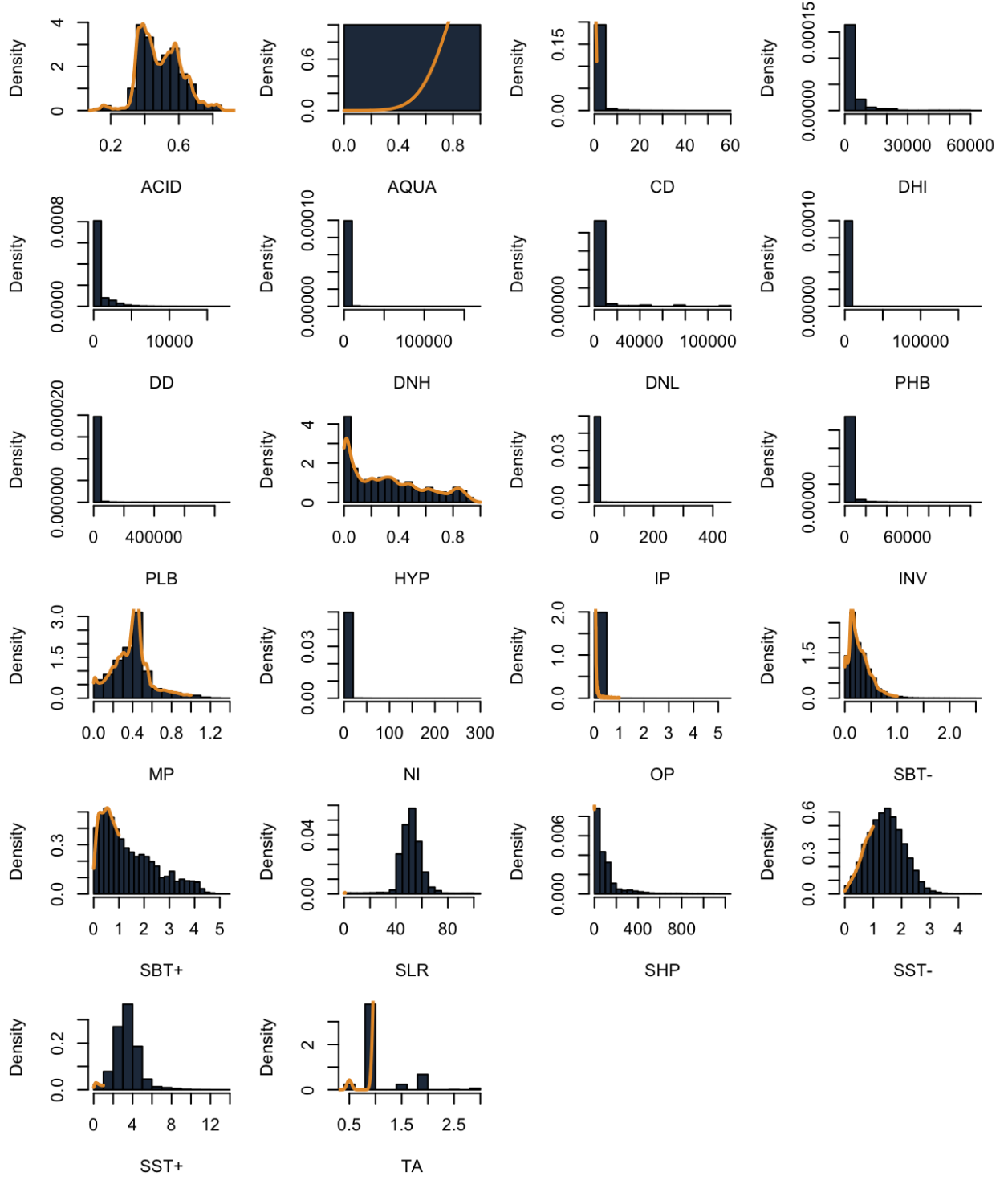


Figure 1: Frequency distribution of the untransformed data for all driver layers.



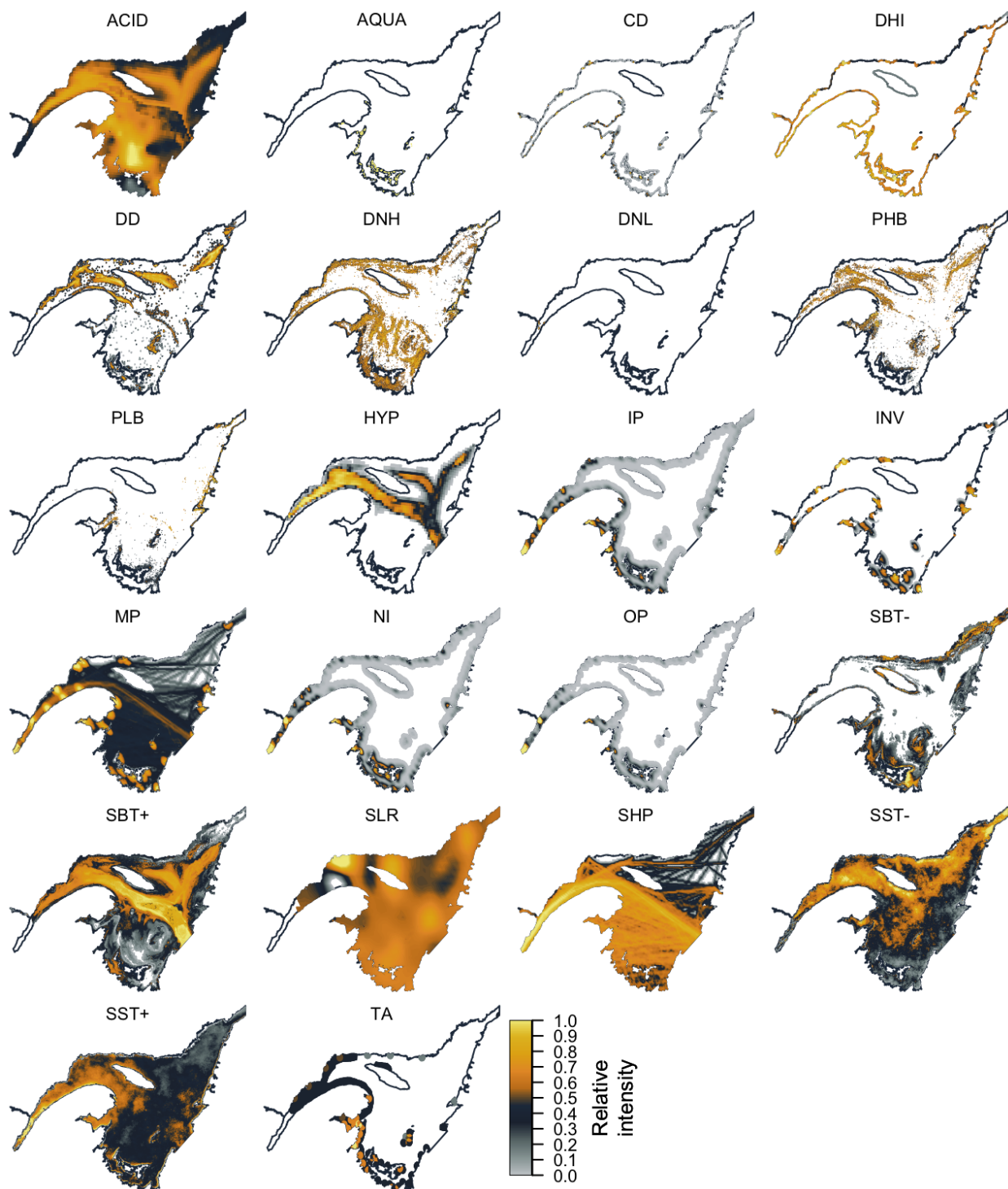


Figure 2: Distribution and intensity of transformed and normalized drivers in the Estuary and Gulf of St. Lawrence available on \*eDrivers\*.

### 3 Cumulative exposure

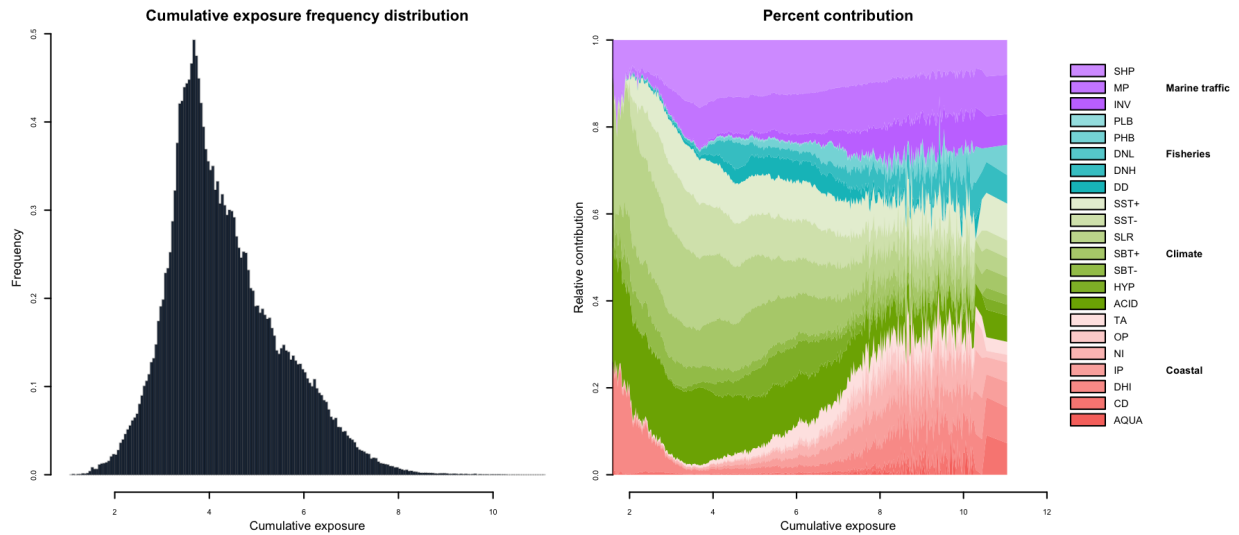


Figure 3: Frequency distribution of cumulative exposure (*i.e.* sum of normalized driver intensity in each grid cell) and percent contribution of each driver to the frequency distribution of cumulative exposure in the Estuary and Gulf of St. Lawrence.

## 4 Threat complexes

### 4.1 Clustering

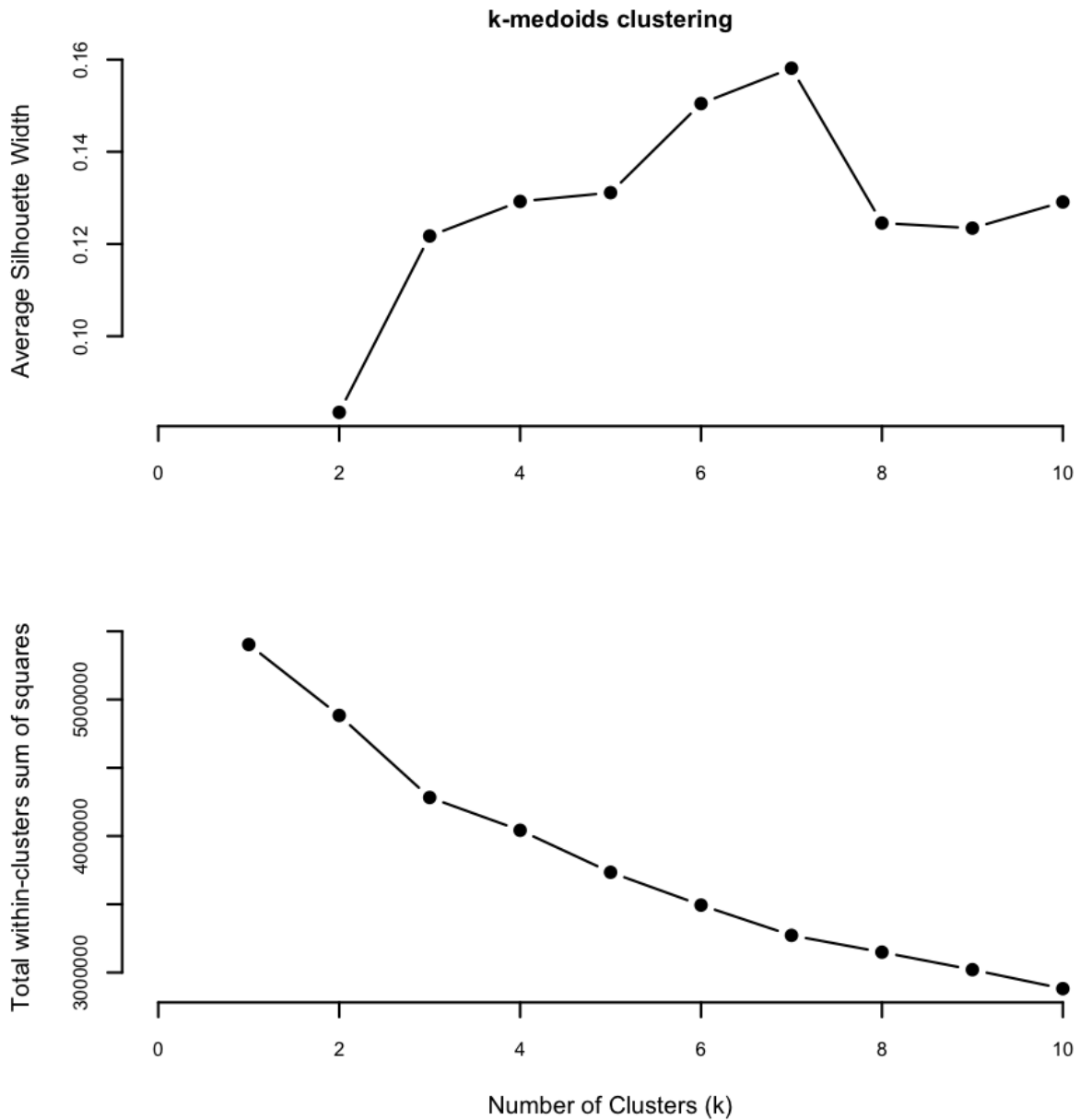


Figure 4: Validation procedure for the *k-medoids* and *k-means* clustering algorithms based on the number of cluster that maximizes average silhouette width (upper panels; Kaufman and Rousseeuw, 1990) and minimizes the total within-cluster sum of squares (WSS; lower panels).

## 4.2 Inter-cluster dissimilarity

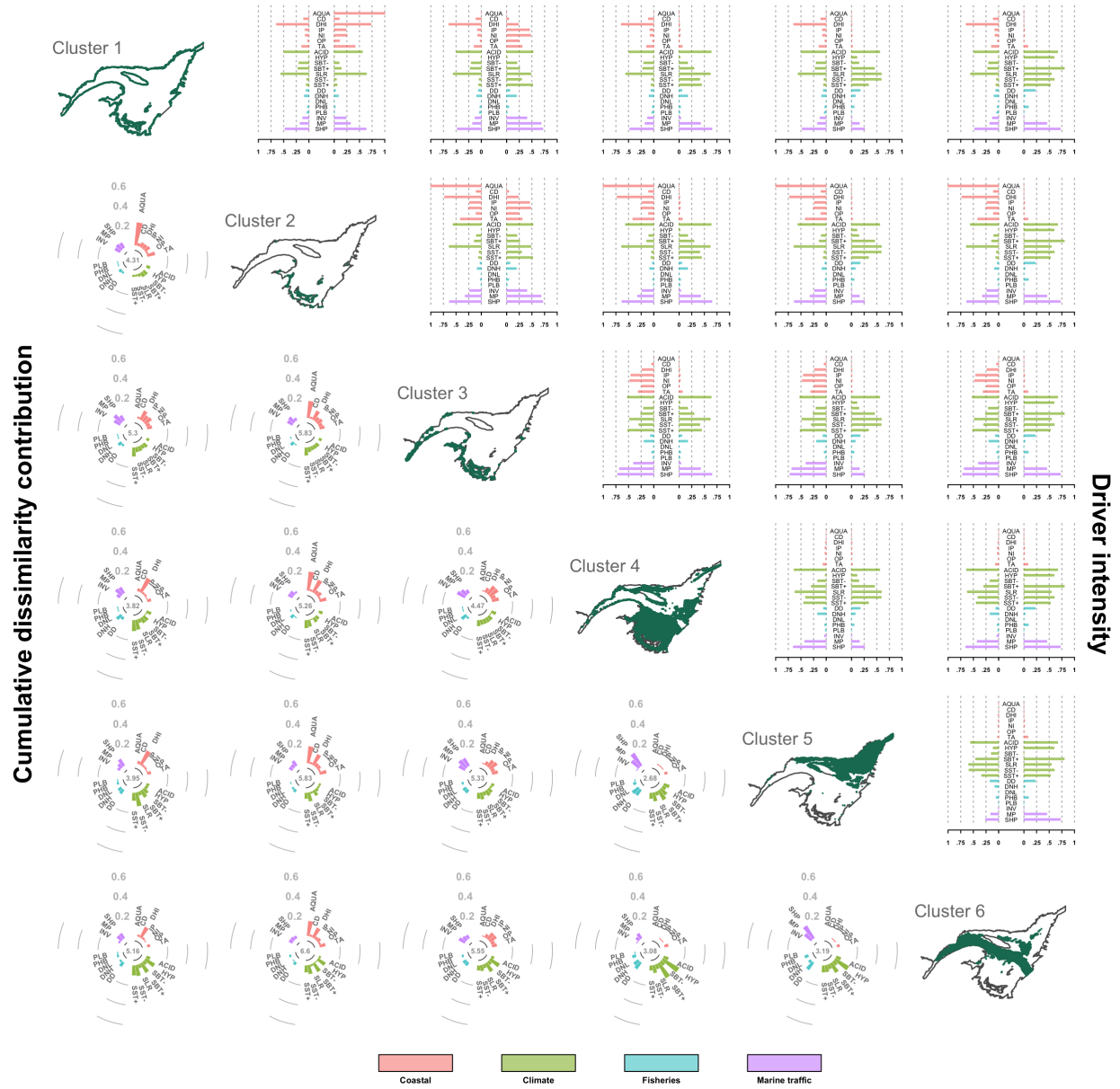


Figure 5: Evaluation of inter-cluster dissimilarity using a similarity percentage analysis (SIMPER) with Manhattan distance (Clarke, 1993). The figure diagonal presents the distribution of the 6 clusters identified using the *k-medoids* clustering algorithm. The lower triangle shows all combinations of inter-cluster dissimilarity with circular barplots showing the percent contribution to total dissimilarity of each driver and with the total inter-cluster dissimilarity in the center of the barplots. The upper triangle shows the average relative intensity of each driver for all driver combinations, with barplots to the left and the right representing the row and columns clusters, respectively.

### 4.3 Intra-cluster similarity

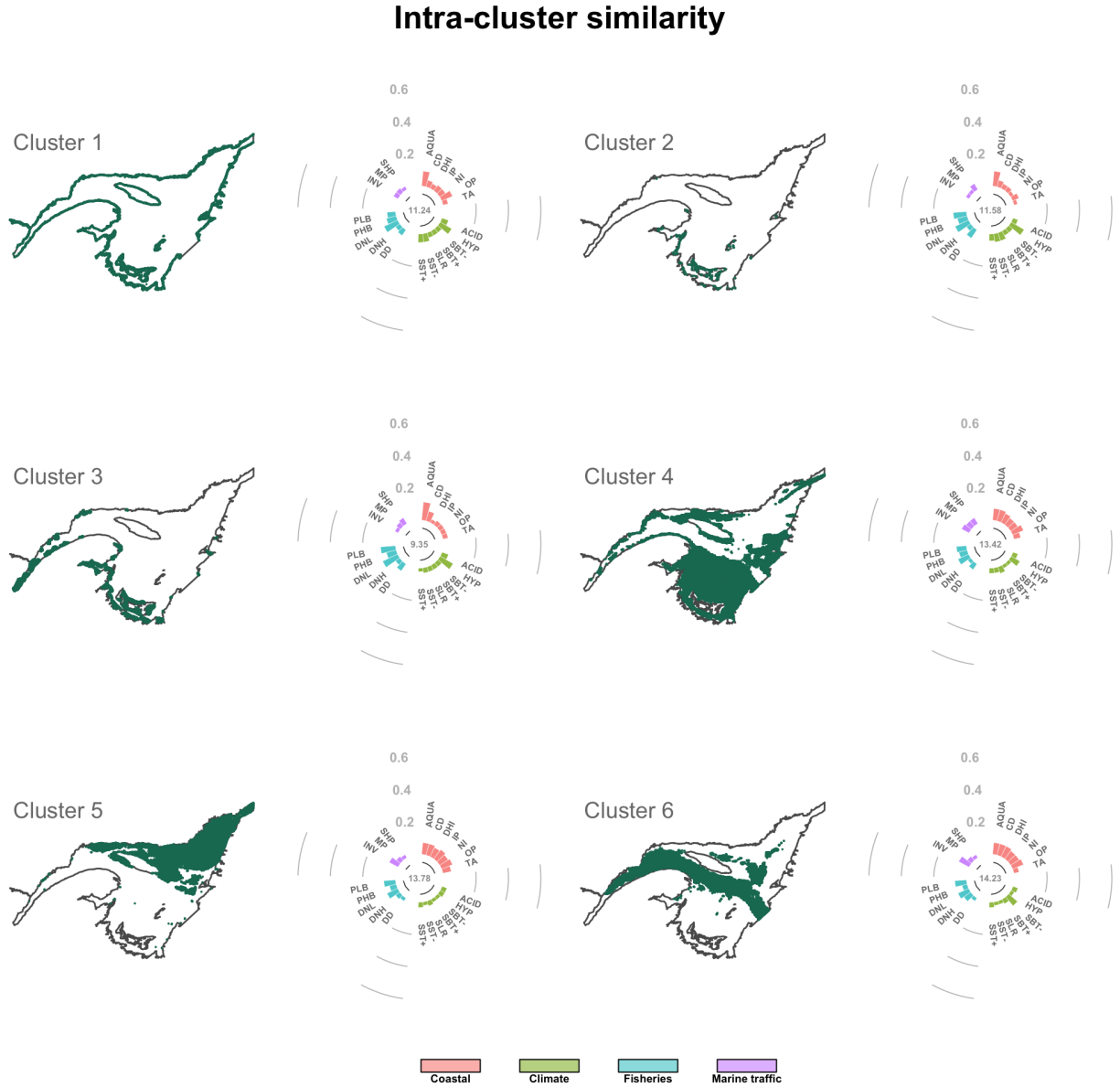


Figure 6: Evaluation of intra-cluster similarity using the Manhattan distance transformed to a similarity index. The distribution of the 6 clusters is presented along with circular barplots showing the percent contribution to total similarity of each driver and with the total intra-cluster similarity in the center of the barplots.

## References

- AAF (2016). Marine Aquaculture Site Mapping Program (MASMP). Department of Agriculture, Aquaculture and Fisheries (AAF), Government of New-Brunswick, New-Brunswick, Canada. Available at: <https://www2.gnb.ca/content/gnb/en/departments/10/aquaculture/content/masmp.html>.
- Bates, S., Beach, D., Comeau, L., Haigh, N., Lewis, N., Locke, A., et al. (2019). Marine harmful algal blooms and phycotoxins of concern to Canada. Can. Tech. Rep. Fish. Aquat. Sci. In revision.
- Blais, M., Galbraith, P. S., Plourde, S., Scarratt, M., Devine, L., and Lehoux, C. (2019). Chemical and Biological Oceanographic Conditions in the Estuary and Gulf of St. Lawrence during 2017. DFO Can. Sci. Advis. Sec. Res. Doc. 2019/009. Iv + 56 p.
- Bourdages, H., Marquis, M.-C., Nozères, C., and Ouellette-Plante, J. (2018). Assessment of northern shrimp stocks in the Estuary and Gulf of St. Lawrence in 2017: Data from the research survey. DFO Can. Sci. Advis. Sec. Res. Doc. 2018/057. Iv + 67 p.
- Bove, C. B., Ries, J. B., Davies, S. W., Westfield, I. T., Umbanhowar, J., and Castillo, K. D. (2019). Common Caribbean corals exhibit highly variable responses to future acidification and warming. *Proceedings of the Royal Society B: Biological Sciences* 286, 20182840. doi:10.1098/rspb.2018.2840.
- Chabot, D., and Claireaux, G. (2008). Environmental hypoxia as a metabolic constraint on fish: The case of Atlantic cod, *Gadus morhua*. *Marine Pollution Bulletin* 57, 287–294. doi:10.1016/j.marpolbul.2008.04.001.
- DFO (2016a). Prince Edward Island Aquaculture Leases. Aquaculture Division. Department of Fisheries and Oceans Canada (DFO). Prince-Edward-Island, Canada. Available at: <http://www.arcgis.com/home/item.html?id=16aa8830c7084a8a92ce066b525978b4>.
- DFO (2016b). Zonal Interchange File Format (ZIFF) data. A compilation of landing data from logbook data between 2010 and 2015. Gestion des données, Institut Maurice Lamontagne, Department of Fisheries and Oceans (DFO) Mont-Joli, Canada.
- Diaz, R. J., and Rosenberg, R. (1995). Marine benthic hypoxia: A review of its ecological effects and the behavioural responses of benthic macrofauna. *Oceanography and Marine Biology. An annual review* 33, 245–303.
- Dickson, A. G., Sabine, C. L., and Christian, J. R. (2007). Guide to Best Practices for Ocean CO2 Measurements. North Pacific Marine Science Organization.

- Dutil, J.-D., Proulx, S., Chouinard, P.-M., and Borcard, D. (2011). A hierarchical classification of the seabed based on physiographic and oceanographic features in the St. Lawrence. *Can. Tech. Rep. Fish. Aquat. Sci.* 2916: Vii + 72 p.
- Dutil, J.-D., Proulx, S., Galbraith, P. S., Chassé, J., Lambert, N., and Laurian, C. (2012). Coastal and epipelagic habitats of the estuary and Gulf of St. Lawrence. *Can. Tech. Rep. Fish. Aquat. Sci.* 3009: Ix + 87 pp.
- Earth observation group (2019). Version 1 VIIRS Day/Night Band Nighttime Lights. NOAA National Centers for Environmental Information (NCEI).
- FA (2016). Aquaculture Site Mapping Tool. Department of Fisheries and Aquaculture (FA), Department of Agriculture, Government of Nova-Scotia. Nova-Scotia, Canada. Available at: <https://novascotia.ca/fish/aquaculture/site-mapping-tool/>.
- Fabry, V. J., Seibel, B. A., Feely, R. A., and Orr, J. C. (2008). Impacts of ocean acidification on marine fauna and ecosystem processes. *ICES Journal of Marine Science* 65, 414–432. doi:10.1093/icesjms/fsn048.
- FFA (2016). Description of aquaculture sites in Newfoundland. Department of Fisheries, Forestry and Agrifoods (FFA), Government of Newfoundland and Labrador. Newfoundland, Canada.
- Galbraith, P. S., Chassé, J., Caverhill, C., Nicot, P., Gilbert, D., Lefaivre, D., et al. (2018). Physical Oceanographic Conditions in the Gulf of St. Lawrence during 2017. DFO Can. Sci. Advis. Sec. Res. Doc. 2018/050. V + 79 p.
- Halpern, B. S., Frazier, M., Potapenko, J., Casey, K. S., Koenig, K., Longo, C., et al. (2015a). Cumulative human impacts: Raw stressor data (2008 and 2013). Knowledge Network for Biocomplexity. doi:10.5063/fls180fs.
- Halpern, B. S., Frazier, M., Potapenko, J., Casey, K. S., Koenig, K., Longo, C., et al. (2015b). Spatial and temporal changes in cumulative human impacts on the world’s ocean. *Nature Communications* 6. doi:10.1038/ncomms8615.
- Halpern, B. S., Walbridge, S., Selkoe, K. A., Kappel, C. V., Micheli, F., D’Agrosa, C., et al. (2008). A Global Map of Human Impact on Marine Ecosystems. *Science* 319, 948–952. doi:10.1126/science.1149345.
- Kleypas, J. A., Feely, R. A., Fabry, V. J., Langdon, C., Sabine, C. L., and Robbins, L. L. (2006). Impacts of Ocean Acidification on Coral Reefs and Other Marine Calcifiers: A Guide for Future Research, report of a workshop held 1820 April 2005, St. Petersburg, FL, sponsored by NSF, NOAA, and the US Geological Survey, 88 pp.

- Kroeker, K. J., Kordas, R. L., Crim, R., Hendriks, I. E., Ramajo, L., Singh, G. S., et al. (2013). Impacts of ocean acidification on marine organisms: Quantifying sensitivities and interaction with warming. *Global Change Biology* 19, 1884–1896. doi:10.1111/gcb.12179.
- Lewis, E., Wallace, D., and Allison, L. J. (1998). Program developed for CO<sub>2</sub> system calculations. Brookhaven National Lab., Dept. of Applied Science, Upton, NY (United States); Oak Ridge National Lab., Carbon Dioxide Information Analysis Center, TN (United States) doi:10.2172/639712.
- MAPAQ (2016). Description des sites maricoles de la province de Québec. Sous-ministériat aux pêches et à l’aquaculture commerciales, Direction régionale des Îles-de-la-Madeleine. Ministère de l’Agriculture, des Pêcheries et de l’Alimentation du Québec (MAPAQ). Québec, Canada.
- Millero, F. J. (1986). The pH of estuarine waters. *Limnology and Oceanography* 31, 839–847. doi:10.4319/lo.1986.31.4.0839.
- Mucci, A., Levasseur, M., Gratton, Y., Martias, C., Scarratt, M., Gilbert, D., et al. (2017). Tidally induced variations of pH at the head of the Laurentian Channel. *Canadian Journal of Fisheries and Aquatic Sciences* 75, 1128–1141. doi:10.1139/cjfas-2017-0007.
- Mucci, A., Starr, M., Gilbert, D., and Sundby, B. (2011). Acidification of Lower St. Lawrence Estuary Bottom Waters. *Atmosphere-Ocean* 49, 206–218. doi:10.1080/07055900.2011.599265.
- Nicholls, R. J., and Cazenave, A. (2010). Sea-Level Rise and Its Impact on Coastal Zones. *Science* 328, 1517–1520. doi:10.1126/science.1185782.
- Starr, M., and Chassé, J. (2019). Distribution of omega aragonite in the Estuary and Gulf of St. Lawrence in eastern Canada. Department of Fisheries and Oceans.
- Statistics-Canada (2017). Population and Dwelling Count Highlight Tables. 2016 Census. Statistics Canada Catalogue no. 98-402-X2016001. Ottawa. Released February 8, 2017. Statistics Canada.
- Tukey, J. W. (1977). *Exploratory Data Analysis*. Reading, Massachusetts: Addison-Wesley.
- Uthicke, S., Ebert, T., Liddy, M., Johansson, C., Fabricius, K. E., and Lamare, M. (2016). Echinometra sea urchins acclimatized to elevated pCO<sub>2</sub> at volcanic vents outperform those under present-day pCO<sub>2</sub> conditions. *Global Change Biology* 22, 2451–2461. doi:10.1111/gcb.13223.
- Walbridge, S. (2013). *Assessing ship movements using volunteered geographic information*. University of California, Santa Barbara.



Zeebe, R. E., and Wolf-Gladrow, D. (2001). *CO<sub>2</sub> in seawater: Equilibrium, kinetics, isotopes*. Gulf Professional Publishing.